ADVANCED MATERIALS
www.advmat.de

Emergent Magnetic States and Tunable Exchange Bias at 3d Nitride Heterointerfaces

Qiao Jin, Qinghua Zhang, He Bai, Amanda Huon, Timothy Charlton, Shengru Chen, Shan Lin, Haitao Hong, Ting Cui, Can Wang, Haizhong Guo, Lin Gu, Tao Zhu, Michael R. Fitzsimmons, Kui-juan Jin, Shanmin Wang,* and Er-Jia Guo**

Interfacial magnetism stimulates the discovery of giant magnetoresistance (MR) and spin–orbital coupling across the heterointerfaces, facilitating the intimate correlation between spin transport and complex magnetic structures. Over decades, functional heterointerfaces composed of nitrides have seldom been explored due to the difficulty in synthesizing high-quality nitride films with correct compositions. Here, the fabrication of single-crystalline ferromagnetic Fe_3N thin films with precisely controlled thicknesses is reported. As film thickness decreases, the magnetization dramatically deteriorates, and the electronic state changes from metallic to insulating. Strikingly, the high-temperature ferromagnetism is maintained in a Fe_3N layer with a thickness down to 2 u.c. (≈8 Å). The MR exhibits a strong in-plane anisotropy; meanwhile, the anomalous Hall resistivity reverses its sign when the Fe_3N layer thickness exceeds 5 u.c. Furthermore, a sizable exchange bias is observed at the interfaces between a ferromagnetic Fe_3N and an antiferromagnetic CrN. The exchange bias field and saturation moment strongly depend on the controllable bending curvature using the cylinder diameter engineering technique, implying the tunable magnetic states under lattice deformation. This work provides a guideline for exploring functional nitride films and applying their interfacial phenomena for innovative perspectives toward practical applications.

1. Introduction

Magnetic materials possessing ultralarge remanent magnetization and small coercive fields are generally useful in the magnetic recording and energy harvest industries, such as motors, generators, and actuators.[1–3] Typically, Fe–Co alloys and compounds containing rare-earth elements (such as Sm and Nd) historically have been chosen for the beforehand applications.[4,5] However, the cost of manufacturing and maintaining such materials is too high for developing highly efficient, compact, and reliable devices for future technologies. Transition metal nitrides (TMNs) are a class of functional materials in which the nitrogen atoms are integrated into the interstitial sites of parent metals.[6–8] Therefore, TMNs exhibit extremely rich physical properties, for instance, high dielectricity,[9,10] high thermal conductivity,[11] superconductivity,[12,13] ferroelectricity,[14–16] as well as

Q. Jin, Q. Zhang, S. Chen, S. Lin, H. Hong, T. Cui, C. Wang, T. Zhu, K.-j. Jin, E.-J. Guo
Beijing National Laboratory for Condensed Matter Physics and Institute of Physics
Chinese Academy of Sciences
Beijing 100190, P. R. China
E-mail: kjjin@iphy.ac.cn; ejguo@iphy.ac.cn

Q. Jin, S. Chen, S. Lin, H. Hong, T. Cui, C. Wang, K.-j. Jin, E.-J. Guo
Department of Physics & Center of Materials Science and Optoelectronics Engineering
University of Chinese Academy of Sciences
Beijing 100049, P. R. China

H. Bai
Spallation Neutron Source Science Center
Dongguan 523803, P. R. China

A. Huon
Department of Physics
Saint Joseph's University
Philadelphia, PA 19131, USA

The ORCID identification number(s) for the author(s) of this article can be found under https://doi.org/10.1002/adma.202208221.

DOI: 10.1002/adma.202208221

T. Charlton, M. R. Fitzsimmons
Neutron Scattering Division
Oak Ridge National Laboratory
Oak Ridge, TN 37831, USA

C. Wang, T. Zhu, K.-j. Jin, E.-J. Guo
Songshan Lake Materials Laboratory
Dongguan, Guangdong 523808, P. R. China

H. Guo
Key Laboratory of Material Physics & School of Physics and Microelectronics
Zhengzhou University
Zhengzhou 450001, P. R. China

L. Gu
National Center for Electron Microscopy in Beijing and School of Materials Science and Engineering
Tsinghua University
Beijing 100084, P. R. China

M. R. Fitzsimmons
Department of Physics and Astronomy
University of Tennessee
Knoxville, TN 37996, USA

S. Wang
Department of Physics
Southern University of Science and Technology
Shenzhen 518055, P. R. China
E-mail: wangsm@sustech.edu.cn

magnetism.[17–19] Except for these remarkable physical properties, the characteristics of superior hardness, corrosion resistance, and antioxidant have made TMNs stable in the air and suitable for coating layers of functional devices.[1–3] Although TMNs have many advantages, the challenges in synthesizing single-crystalline TMN thin films with high crystallinity and correct chemical composition have hindered the research on their intrinsic properties and intriguing interfacial phenomena. Taking iron nitrides as an example, $Fe_{16}N_2$ has been theoretically predicted as one of the most promising rare-earth-free strong magnet candidates with a giant saturation moment (≈3.5 μ_B/Fe), which is 36% larger than that of a single-crystalline iron (≈2.2 μ_B/Fe).[20,21] Increasing the nitrogen content, Fe_3N exhibits ferromagnetism with a slightly reduced saturation moment. Due to its ultralarge spin polarization, it holds potential applications in magnetic tunneling junctions and spin-polarized light-emitting diodes.[22–27] However, Fe_3N often appears in other iron nitride forms due to the close thermally stable energy. The magnetic and electrical properties of Fe_3N can be greatly influenced by impurities, chemical disorders, and nitrogen vacancies (NVs).[28] Currently, most work mainly focuses on amorphous, polycrystalline, and nanoparticle nitrides.[22–28] The sample quality hinders the deep investigation of their intrinsic properties in their thin film form. Therefore, mastering the advanced preparation methods of TMN magnetic films with the accurate stoichiometric ratio is particularly important to understand the structure of objective substances and investigate the coupling mechanism between spin and other degrees of freedom. These factors are the core constraints restricting the practical applications of these excellent magnetic materials.

Previously, most TMN thin films were fabricated by reactive magnetron sputtering, radiofrequency nitrogen plasma-assisted molecular beam epitaxy, or metal–organic chemical vapor deposition.[29–31] The crystallinity is relatively poor because of the formation of polycrystalline grains and NVs. Recently, our group reported the fabrication of high-crystalline stoichiometric CrN ultrathin films using the pulsed laser deposition (PLD) technique.[32–35] The specimens were prepared by laser ablating from a high-pressure synthesized stoichiometric target and compensating the NVs using an in situ atomic nitrogen plasma source. The CrN thin films fabricated in this manner exhibited a paramagnetic-to-antiferromagnetic transition at a temperature close to its bulk value ≈283 K,[36,37] indicating the correct stoichiometry of high-quality CrN films. Thus, depending on the thickness, orientation, stacking sequence, and emergent interfacial phenomena, their intrinsic physical properties could be explored in a controlled manner,[32–35] similar to the extensively investigated transition metal oxides.

In this work, we report the fabrication of stoichiometric single-crystalline Fe_3N thin films and the integration of antiferromagnetic CrN films with atomically sharp interfaces. The thickness-dependent magnetic and electrical phase transitions were observed. When the thickness was reduced to 2 unit cells (u.c.), the ferromagnetic ground state of a Fe_3N film was maintained. We observed a significant anomaly in the out-of-plane magnetic hysteresis loops depending on the film thickness and temperature, which may be attributed to the reorientation of canted spins. We noted that the magnetic properties of a freestanding Fe_3N/CrN bilayer were extremely sensitive (≈2680 emu cm^{-3} per mm^{-1}) to the bending stress, providing an innovative design strategy for uniaxial-strain sensors.

2. Results and Discussion

The nitridation of iron leads to a variety of phases, strongly depending on the nitrogen content. Among them, ε-phase Fe_3N (ε-Fe_3N, abbreviation Fe_3N thereafter) exhibits interesting magnetic states and extends over a wide range of the phase diagram.[38] A typical crystallized form of Fe_3N is presented in **Figure 1**a. A succession of Fe–N layers is arranged along the *c* axis with N layers as spacers between Fe layers, resulting in an out-of-plane lattice constant of 4.38 Å. When viewed from the [001] direction, Fe_3N consists of alternating atomic planes of Fe^{3+} and N^{3-} ions with a buckled hexagonal structure (Figure 1b). The atomic arrangement of Fe_3N is similar to that of a (0001) surface of α-Al_2O_3 (point group *R*-3*c*) (Figure 1c). The lattice constants of Fe_3N and α-Al_2O_3 are very close, yielding a moderate lattice mismatch of –1.8%. The similar crystal symmetry and relatively small lattice mismatch enable the epitaxial fabrication of ε-phase Fe_3N films on the α-Al_2O_3 substrates using the plasma-assisted PLD technique. The highly reactive N atoms in situ generated by a radio-frequency plasma source compensate the NVs during the growth. This process guarantees the correct stoichiometry of Fe_3N films. Microstructures around the interfaces between Fe_3N and α-Al_2O_3 are shown in Figure 1d, performed by scanning transmission electron microscopy (STEM) in the high-angle annular dark-field (HAADF) mode. The STEM image indicates the high crystallinity of Fe_3N single layers, and the sample is free of obvious defects. The HAADF-STEM image confirms the epitaxial growth of Fe_3N on the substrates with atomically sharp interfaces. To note, we observed an ultrathin transition layer with a thickness of ≈1 nm (marked in yellow arrows) between Fe_3N and α-Al_2O_3. This fact can be attributed to the accommodation of misfit strain. The Fe_3N films need to preserve a structural transition to their lattice; thus, building up a slightly disordered region between film and substrate. Nevertheless, the overall Fe_3N structure was well-maintained without hinting at severe structural disorders or impurity phases within the films. Detailed information about the transition layer can be further understood by more extensive studies utilizing elemental-specific atomic resolution electron energy loss spectroscopy (EELS), which we leave out as an important future study. The inset of Figure 1d on the upper right shows the high-magnified STEM image of a region in Fe_3N. The bright features indicate the positions of Fe atom columns, matching well with the atomic structure of single-phase ε-Fe_3N.[39] The light element N cannot be observed clearly in these STEM images due to the small atomic number (*Z*).

X-ray diffraction (XRD) measurements were carried out on a Panalytical MRD diffractometer equipped with a monochromator (only $K\alpha_1$ is allowed, $\lambda = 1.54$ Å). The film thickness was controlled by counting the number of laser pulses, further confirmed by X-ray reflectivity (Figure S1, Supporting Information). Figure 1e shows the XRD θ–2θ scans for a 30-u.c.-thick Fe_3N on α-Al_2O_3 substrates. Only 00*l* reflections from both films and

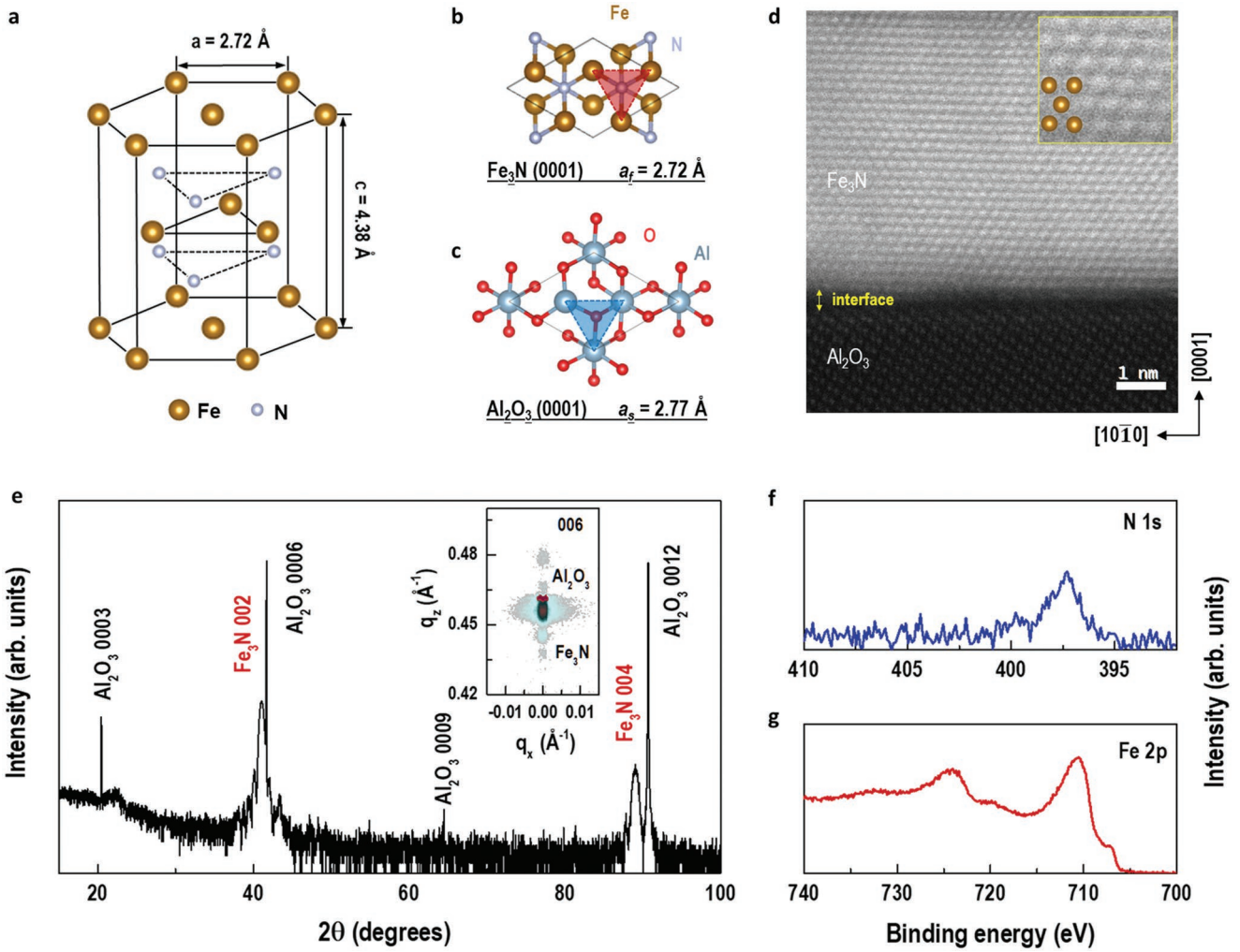

Figure 1. Structure and electronic state characterizations of single crystalline Fe_3N films. a) Schematic of a Fe_3N single unit cell. b,c) Top-views of Fe_3N and Al_2O_3 lattice structures, respectively, yielding to highly compatible group symmetry and relatively small misfit strain of ≈–1.8%. d) Atomic-resolved STEM image across the Fe_3N/Al_2O_3 interface. Inset shows a representative zoom-in STEM image with atomic structures. e) XRD θ–2θ scan of a 30-u.c.-thick Fe_3N film. The inset of (e) shows the RSM around the 006 reflection of Al_2O_3 substrate. f,g) N 1s and Fe 2p core-level XPS of a typical Fe_3N single film, confirming the presence of sufficient nitrogen content.

substrates were observed, suggesting the epitaxial growth of Fe_3N films. The inset of Figure 1e presents a reciprocal space map around substrates' 006 reflections. The clear Kiessig fringes up to three orders together with a narrow rocking curve at Fe_3N 002 reflection with full width at half maximum of ≈0.03° (not shown) indicate the high crystallinity of as-grown Fe_3N films. We determined that the out-of-plane lattice constant of a 30-u.c.-thick Fe_3N was ≈4.38 Å, close to its bulk value. Also, the lattice constant did not vary greatly, further decreasing the layer thickness to 10 u.c. The relaxation of epitaxial misfit strain is attributed to the sharp structural transition at interfaces by forming a nanometer-thick transition layer (Figure 1d). XPS analysis of Fe_3N films was carried out by investigating N 1s (Figure 1f) and Fe 2p (Figure 1g) core level spectra. The binding energy was carefully calibrated by taking C 1s peak at 284.6 eV as a reference. Only one main peak centered at 397.4 eV was observed, corresponding to N 1s state due to the N content in Fe_3N. The prominent components of Fe 2p peaks at 710 and 725 eV indicate hybridization between Fe and N. We notice that there were two weak pre-peaks at 706 and 720 eV, which may be associated with metallic unbonded Fe termination layers on the top surface.[40]

The magnetic and electrical transport properties of Fe_3N films were investigated as a function of film thickness. **Figures 2**a and 2b show the temperature-dependent magnetization (M) and resistivity (ρ) of 6-u.c.- and 30-u.c.-thick Fe_3N films, respectively. M–T and ρ–T curves for Fe_3N single films with various film thicknesses are shown in Figure S2, Supporting Information. Thickness-dependent Curie temperature (T_C), saturation moment (M_S), and ρ_{300K} are summarized in Figures 2e–g, respectively. T_C of a 30-u.c.-thick Fe_3N film was ≈440 K and reduced to ≈385 K for a 2-u.c.-thick Fe_3N film. Accompanied by the T_C reduction, M_S of Fe_3N films was dramatically reduced by decreasing the thickness below 10 u.c. (Figure 2c). Surprisingly, we found that M_S of a 2-u.c.-thick Fe_3N film was ≈150 emu cm^{-3}. In fact, this saturation moment

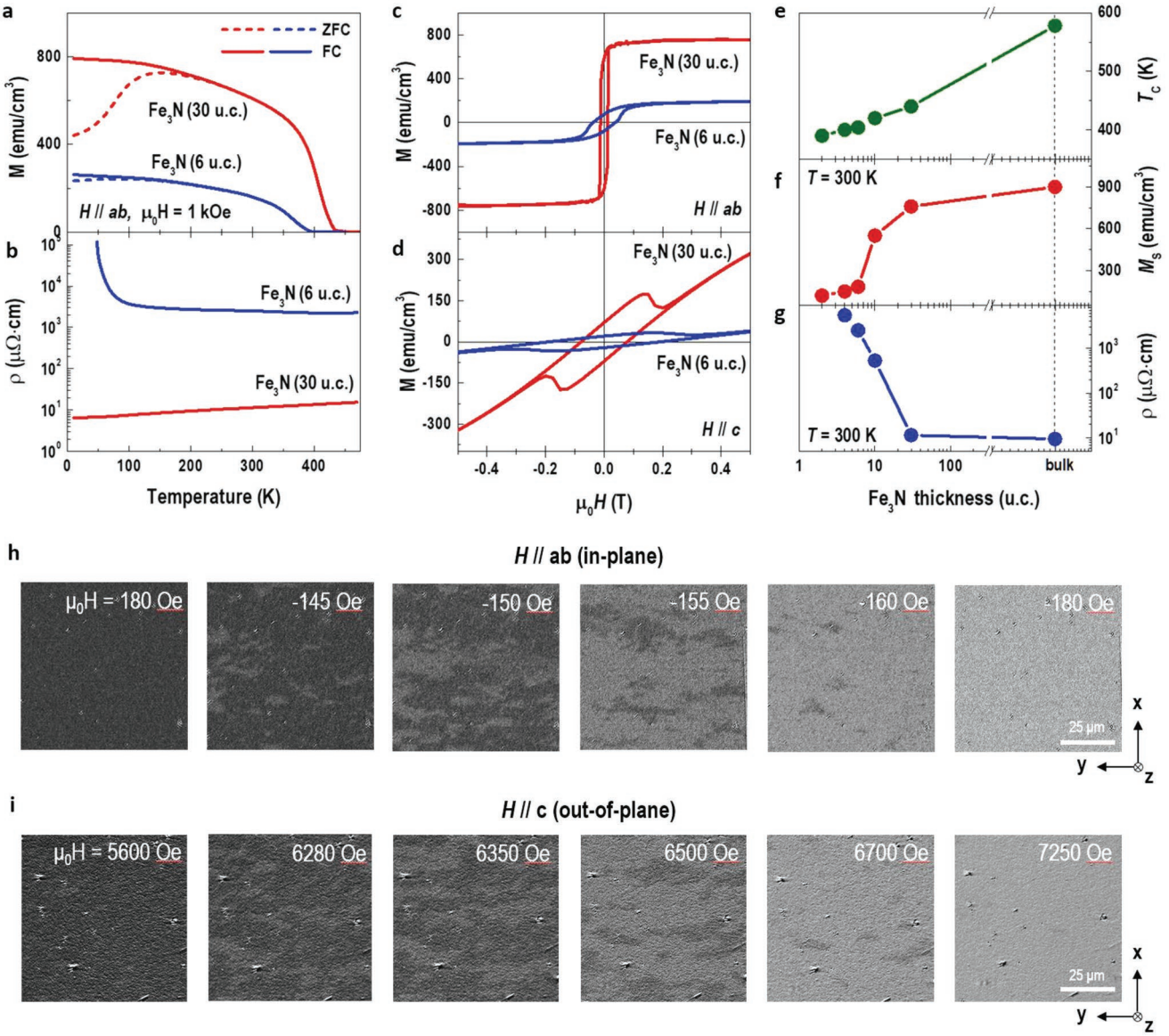

Figure 2. Thickness dependent magnetic and transport properties of Fe_3N single films. a,b) Temperature-dependent magnetization and resistivity of 6-u.c.- and 30-u.c.-thick Fe_3N films, respectively. c,d) Field-dependent magnetization of 6-u.c.- and 30-u.c.-thick Fe_3N films when magnetic field is applied along in-plane ($H//ab$) and out-of-plane ($H//c$) direction, respectively. e) Curie temperature (T_c), f) room-temperature saturation magnetization (M_s), and g) resistivity (ρ) as a function of Fe_3N film thickness. h,i) MOKE images for a 30-u.c.-thick Fe_3N film with magnetic fields applied along the in-plane and out-of-plane direction at room temperature, respectively. The dark contrast represents the magnetization along the y (or z) axis, and light contrast represents the magnetization along the $-y$ (or $-z$) axis when the magnetic field is applied along the in-plane (or out-of-plane) direction.

at subnanometer thickness is much larger than those of most correlated magnetic oxides and nitride films. The Fe_3N film growth with a thickness below 2 u.c. is relatively challenging because of the nitrogen-to-oxygen substitutions at the surface. The Fe oxidization would result in a possible ferromagnetic state change of Fe_3N to the antiferromagnetic state of Fe_2O_3. This reaction seems unavoidable without a proper capping layer. For the transport behavior of Fe_3N films, we observed a clear metal-to-insulator transition by decreasing the film thickness. For a 30-u.c.-thick Fe_3N single film, a metallic phase was maintained at all temperatures. Please note that ρ_{300K} of a 30-u.c.-thick Fe_3N was only 9.5 μΩ cm, comparable to those of most noble metals, for instance, Pt (ρ_{300K} = 10.6 μΩ cm) and Au (ρ_{300K} = 2.2 μΩ cm).[41,42] However, when the thickness fell below 10 u. c, the Fe_3N films were changed into an insulator with a sharp resistivity increase by four orders of magnitude. The dimensional confinement-induced metal-to-insulator transition has been reported previously in both correlated oxides and nitrides.[32,43–47] Many mechanisms have been proposed to explain the critical thickness for metallic conduction, including local structural distortion, interfacial charge imbalance, or orbital ordering. In our case, a plausible interpretation of this phenomenon was weak localization, where quantum interference of electronic waves diffusing around impurities enhanced

backscattering and thus led to a conductivity reduction. We modeled the low-temperature transport property of a 6-u.c.-thick Fe_3N film. It can be well-described using variable-range hopping conduction mechanism involving electron–electron interactions.[48] In this ultrathin limit, although many Fe atoms persist in the Fe_3N films, the conducting environment is different from a bulk-like environment for nearest-neighbor hopping along the surface normal direction, ultimately driving its conductivity to the incipient order of the 2D limit.

The magnetic easy-axis of Fe_3N films aligned in the film plane, similar to most strongly correlated thin films. The coercive field (H_C) increased on film thickness reduction (Figure 2c). Figure 2d shows the magnetic hysteresis loops of 6-u.c.- and 30-u.c.-thick Fe_3N films when $H//c$. We observed a consistent anomaly in all M–H loops of Fe_3N films with different film thicknesses. As sweeping magnetic fields from positive to negative values, the moment first linearly reduced and then abnormally increased at ≈0.2 T. As the magnetic field was further reduced, the moment decreased monotonically. This behavior has seldom been observed in other magnetic TMN thin films. To ensure consistency, we record this anomaly in the M–H loops of a 30-u.c.-thick Fe_3N film as a function of temperature (Figure S3, Supporting Information). The maximum moment at ≈0.1–0.2 T, as well as the coercive field, continuously decreased as temperature increased. We performed the magneto–optical Kerr effect (MOKE) measurements on a 30-u.c.-thick Fe_3N film. Figures 2h and 2i show two typical field-dependent evolutions of magnetic domain patterns captured by MOKE when $H//ab$ and $H//c$, respectively. The white areas represent the magnetic domains, with a negative magnetization ($M < 0$) created by applying a negative field to positively saturated films with $M > 0$ (black areas). The density of effective nucleation sites in our films was relatively low, indicating a rather high homogeneity of samples. Please note that the switching field along the in-plane direction was an order of magnitude smaller than that along the out-of-plane direction. Therefore, we hypothesized that the anomaly in M–H loops ($H//c$) was attributed to the reorientation of Fe spins from in-plane to out-of-plane through a metastable state, where the partial magnetic domains aligned in the film plane during field-switching. The magnetoresistance (MR) of 6 u.c.- and 30-u.c.-thick Fe_3N films were measured as a function of temperature and magnetic field (Figures S4–S6, Supporting Information). MR of both samples exhibited the butterfly hysteresis loops at small fields, which are coupled with H_C as comparatively shown in Figure 2c,d. Comparing MR at high fields indicates that both Fe_3N films had negative linear responses that increased systematically in magnitude with temperature decrement. Interestingly, we observed a strong in-plane anisotropy in MR strongly depending on the current direction when $H//c$. For a 30-u.c.-thick Fe_3N film, the MR($I//a$) was opposite to MR($I//b$). However, when the thickness of Fe_3N films was reduced to 6 u.c., MR trends for both current directions were similar. We believe that the interesting magnetotransport behaviors were caused by the anisotropic spin alignments confined by its lattice structure. These results are consistent with the typical results for ferromagnets possessing strong in-plane anisotropy.

Furthermore, we investigated the magnetic exchange coupling at the interfaces between ferromagnetic Fe_3N and antiferromagnetic CrN layers. **Figure 3**a shows the HAADF-STEM image of a Fe_3N/CrN bilayer. The bright layer indicates the Fe_3N layer, while the dark layer is the CrN layer because the scattering intensity of the HAADF-STEM image was approximately proportional to the square of the atomic number, and meanwhile, the stacking density was higher in the Fe_3N layer. This result reveals that both layers were flat and continuous over long lateral distances, suggesting the formation of high-quality interfaces. The high-magnification image around the Fe_3N/CrN interface (Figure 3b) and compositional EELS maps (Figure 3c–f) obtained from the analysis of the Fe $L_{3,2}$-, Cr $L_{3,2}$-, N *K*-, and O *K*-edge signals revealed both layers that were epitaxially grown and chemically uniformed, as well as the interfaces that were atomically sharp and contained negligible chemical intermixing.The chemical and magnetization distributions across the entire sample were first examined using the polarized neutron reflection (PNR) technique. The measurements were conducted at 10 K after field cooling at 1 T from room temperature. The specular neutron reflectivities are plotted in Figure 3g as a function of wave factor ($q = 4\pi\sin\theta_i/\lambda$) for the spin-up ($R^+$) and spin-down ($R^-$) polarized neutrons, where θ_i is the incident angle, and λ is the wavelength of incident neutrons. The solid lines are the best fits to the experimental data (open symbols). The figure of merit (FOM) of PNR fit yields a value of 1.89. Figure 3h shows the calculated spin asymmetry and its corresponding fit, from which the chemical (Figure 3i) and magnetization (Figure 3j) depth profiles can be obtained. The atomic density of the Fe_3N layer was larger than that of the CrN layer. We found that the CrN layer was separated into two parts: an interface layer and a top layer. The density of the CrN interface layer was slightly smaller than its bulk value. This is possibly due to the strain compensation between dissimilar structural materials. The magnetic depth profile indicates that the Fe_3N layer exhibited a large magnetization (≈1000 emu cm^{-3}) and slightly deteriorated when it was close to the CrN layer. We also noticed that the CrN interface layer showed a small net moment of ≈54 emu cm^{-3} after field cooling. The existence of nonzero moment in the CrN interface layer was robust because the PNR fit with the constraint of zero or negative M in the CrN interface layer had a large deviation from the experiment data, yielding FOM of 4.3 and 5.6, respectively. The field-cooled PNR data suggest that the CrN interface layer was magnetized due to the spins of Cr ions and were pinned to those of Fe ions during the field cooling.[49,50] The magnetization integrated over the entire depth profile obtained from PNR was in good quantitative agreement with the magnetometry data.

The unique transport properties were measured across the Fe_3N/CrN interfaces from $[(CrN)_n/(Fe_3N)_n]_5$ (C_n/F_n) superlattices, where n represents the number of unit cells of Fe_3N and CrN layers, and five is the stacking periodicity of superlattices. Prior to the transport measurements, we performed the room-temperature PNR measurements on two representative C_5/F_5 and C_{10}/F_{10} superlattices (Figures S7 and S8, Supporting Information). These results demonstrated the uniformities of chemical and magnetization distributions within Fe_3N layers. The averaged saturation magnetization of Fe_3N layers in C_5/F_5 was nearly identical to those of Fe_3N layers in C_{10}/F_{10}. MR of C_n/F_n superlattices was recorded by applying currents along the a and b directions at various temperatures. **Figure 4**a–f

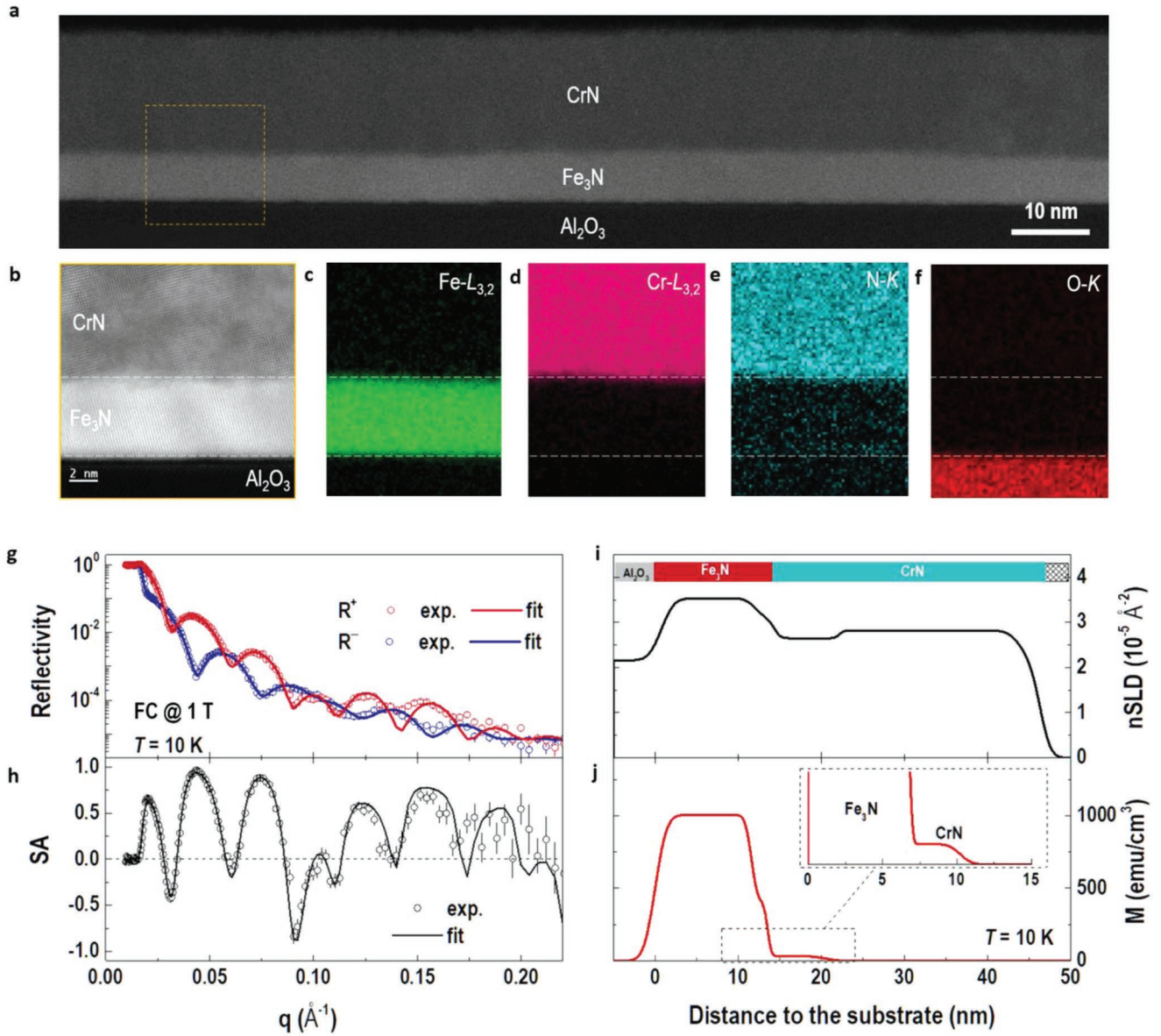

Figure 3. Chemical and magnetization depth profiles across CrN/Fe_3N interface. a) Low-magnication STEM image of a CrN/Fe_3N bilayer grown on Al_2O_3 substrates. b) A high-magnication STEM image across CrN/Fe_3N/Al_2O_3 interfaces marked with the yellow dashed square in (a). c–f) Spatially resolved EELS maps taken at the Fe *L*-, Cr *L*-, N *K*-, and O *K*-edges, respectively. The EELS results clearly indicate the uniformed chemical distribution and atomically sharp interfaces with a minimum chemical intermixing. g) Neutron reflectivities of a CrN/Fe_3N bilayer as a function of wave factor (q). The open symbols (or lines) represent the reflectivities of experiment data (or best fits). h) Calculated spin asymmetry (SA) from $(R^+ - R^-)/(R^+ + R^-)$. Open symbols and solid line are experimental data and best fit, respectively. i,j) Nuclear scattering length density (nSLD) and magnetization depth profiles, respectively. The inset of (j) shows the zoom-in magnetization depth profile across the interface between CrN and Fe_3N.

shows MRs at 10 K when $H//c$. We noticed that MR did not show a significant difference as a function of the applied field when n was below 5 u.c. However, when n was beyond 5 u.c., the degeneracy of MR between two current directions appeared. Figure 4g,h shows the contour plots of MR when $I//a$ and $I//b$ as a function of layer thickness and temperature. At low temperatures, the MR changed from negative to positive values at a critical thickness (t), and t reduced as further the temperature increased. The strong temperature dependency in MR became subtle for thick layers. Furthermore, we also measured the Hall resistivity (ρ_{xy}) of C_n/F_n superlattices when $H//c$ to probe the intriguing magnetic properties across the interfaces. We subtracted the ordinary Hall resistivity (R_0H) from ρ_{xy} to separate the anomalous Hall effect (AHE) from Hall resistiv. Figure 4i–n shows the field-dependent ($\rho_{xy} - R_0H$) from C_n/F_n superlattices at 10 K. A saturation ($\rho_{xy} - R_0H$) appeared for each C_n/F_n superlattice above a critical field. For n = 2–4, the square-like open hysteresis loops were observed, but the ($\rho_{xy} - R_0H$) value was negative. When n was above 5, we observed a sign reversal from negative to positive in ($\rho_{xy} - R_0H$) at 3 T. As further n increased, ($\rho_{xy} - R_0H$) increased approximately linearly. Since the saturation magnetizations were almost identical in

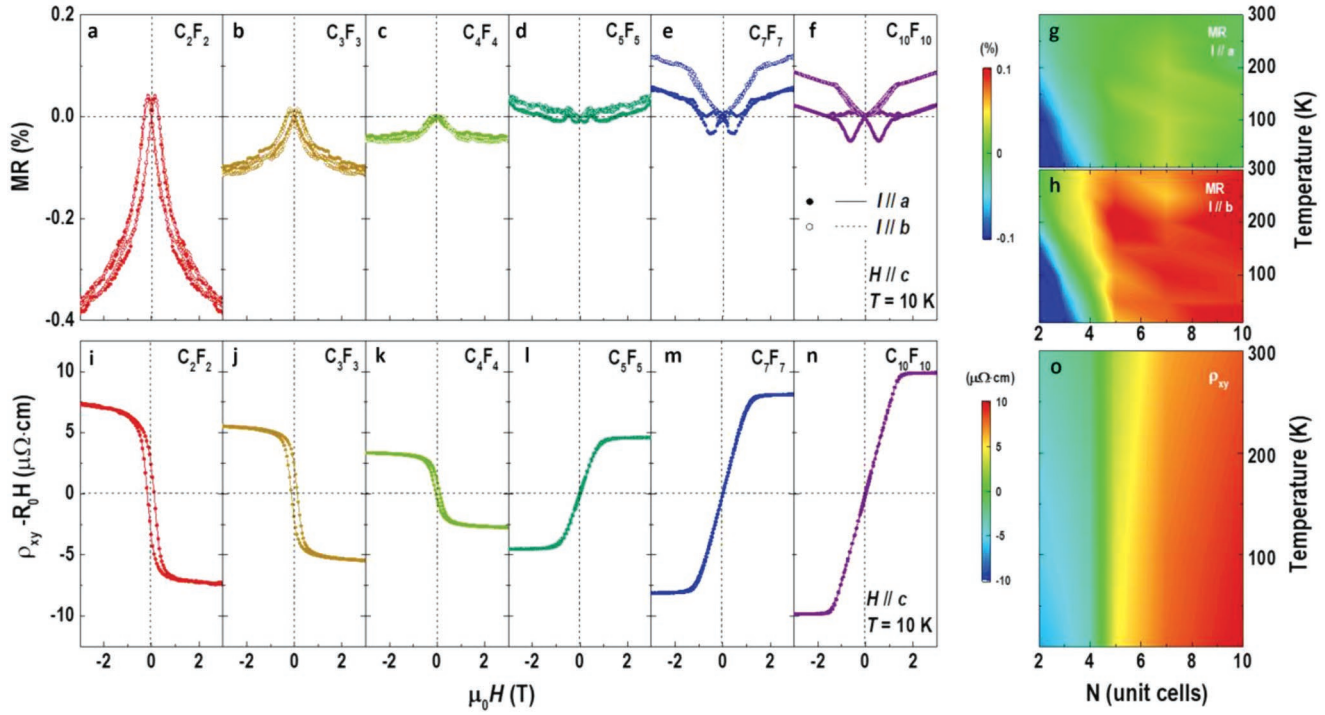

Figure 4. Electrical transport across the $[(CrN)_n/(Fe_3N)_n]$ (C_nF_n) interfaces, where n represents the number of unit cells in the individual layer. a–f) Magnetoresistance (MR) of C_nF_n superlattices as a function of magnetic field at 10 K. The magnetic fields were applied perpendicular to the film plane. The currents were applied in parallel to *a* (solid symbols) and *b* (open symbols) orientations. g,h) MR as a function of temperature and unit cell numbers when the current was applied in parallel to *a* and *b* orientation, respectively. i–n) Anomalous Hall resistivity ($\rho_{xy} - R_0H$) of C_nF_n superlattices as a function of magnetic field at 10 K. o) $\rho_{xy} - R_0H$ as function of temperature and unit cell numbers. For the Hall measurements, the magnetic field was applied along the surface plane.

C_n/F_n ($n > 5$) superlattices, we attributed that the thickness-driven AHE signal reversal possibly originated from the band topology (e.g., the number of crossing points) and was associated with *k*-space Berry curvature.[51] However, we did not observe the typical hump-like topological Hall signals existing in other ferromagnetic metallic systems.[52] Figure 4o shows the ($\rho_{xy} - R_0H$) reduced toward zero as gradually increasing temperature for all C_n/F_n superlattices. Temperature-driven AHE reduction can be understood by the slight Fermi level shift with respect to the avoided band crossing points. It is worth noting that the present spatial magnetic measurements could not detect sub-micrometer-scale magnetic domains (e.g., chiral magnetic bubble-like or skyrmions) in Fe_3N single films or C_n/F_n superlattices across the critical thickness. Further measurements using either magnetic force microscopy[53,54] or Lorentz transmission electron microscopy[55] are needed to identify the nanoscale magnetic domains and possible existing room-temperature skyrmions in such systems.

Besides the intriguing thickness-sensitive magnetotransport behaviors toward the spintronic applications, we further demonstrated that the exchange coupling across the Fe_3N/CrN interface was highly tunable to the mechanical bending stress. We fabricated the Fe_3N/CrN freestanding membranes using water-soluble single-crystalline sodium chloride substrates. We first compared the saturation moment of an as-grown Fe_3N/CrN bilayer on a rigid substrate and a bilayer membrane. A slight increment of the moment of ≈100 emu cm^{-3} in the Fe_3N/CrN membrane was attributed to the removal of substrate constrain. The Fe_3N/CrN membranes attached firmly to the sapphire cylinders with predetermined curvatures ranging from 0 to 0.25 mm^{-1}. The variations of bending curvature led to the successful tuning of lattice deformation.[56–58] We could deliver a roughly linear relationship between the bending stress and the cylinder curvature (R). The membrane support on cylinders with larger R will suffer from a larger lattice deformation. **Figure 5**a shows M–H loops of an as-grown Fe_3N/CrN membrane with R = 0 at 10 K. The magnetic hysteresis exhibited open loops with its center shifted to negative (positive) fields by an exchange bias field (H_{EB}) of ≈115 Oe after 3 T (−3 T) field cooling from room temperature. This behavior suggests the presence of exchange coupling in the antiferromagnetic/ferromagnetic systems. As R increases from 0 to 0.25 mm^{-1}, H_{EB} increased from 115 to 350 Oe, whereas the magnitude of M_S dramatically reduced from 950 to 280 emu cm^{-2} (Figure 5b–d). The ratio between the bending curvatures and M_S was ≈2680 emu cm^{-3} per mm^{-1}, demonstrating a significant advantage of applying such a system for detecting microdeformations. Figures 5e and 5f summarizes the curvature- and temperature-dependent H_{EB} and M_S, respectively. We found that H_{EB} reduced with increasing temperature and reached zero value at the blocking temperature (T_B) ≈150 K (Figure S9, Supporting Information), consistent with the T_N of antiferromagnetic CrN layers.[32–35] The transition temperature of H_{EB} shifted to a high temperature as R increases. This strategy provides a convenient

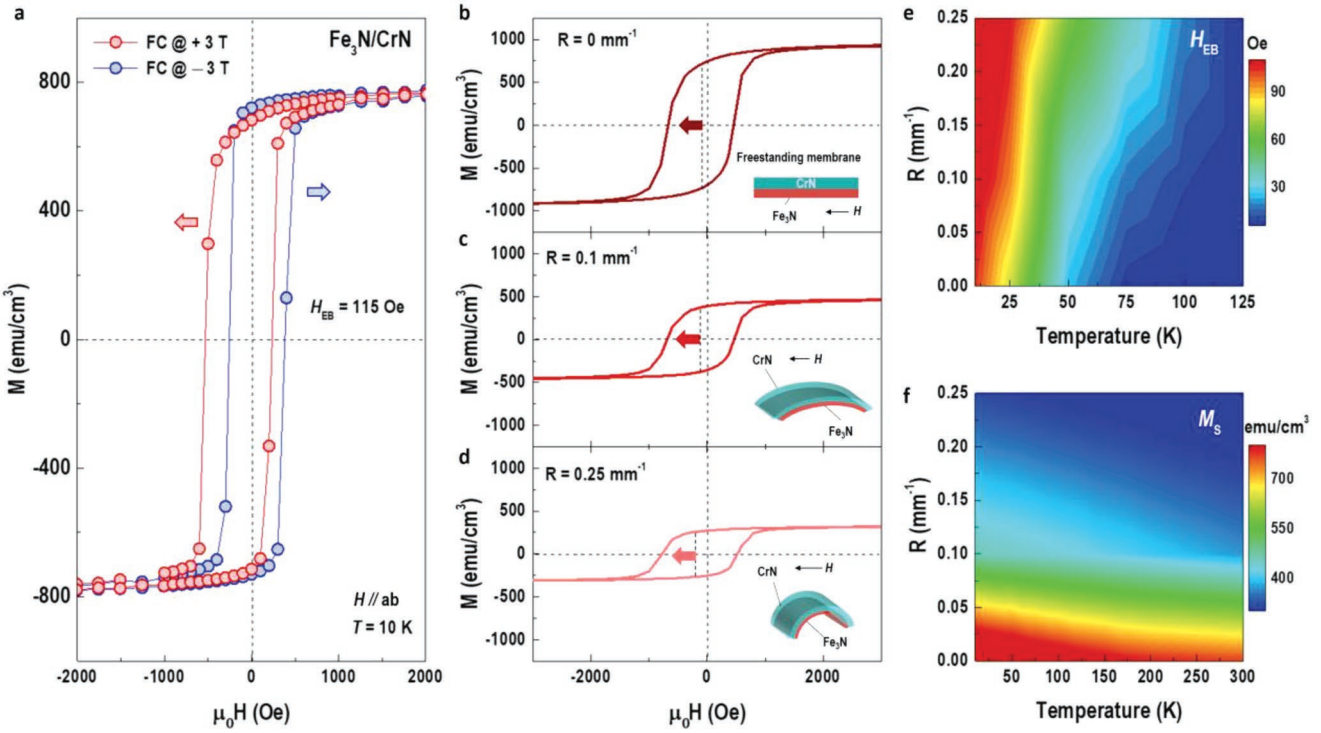

Figure 5. Tunable magnetic states at the CrN/Fe_3N interfaces under bending stress. a) Exchange bias at the CrN/Fe_3N interface at 10 K. The red and blue curves are magnetic hysteresis loops after 3 and −3 T, respectively. b–d) Room-temperature in-plane *M*–*H* loops when a freestanding CrN/Fe_3N bilayer was bended with a curvature of 0, 0.1, and 0.25 mm^{-1}, respectively. e) Exchange bias field (H_{EB}) and f) saturation magnetization (M_S) as a function of temperature and bending curvature.

and continuous way to tune the magnetic properties of freestanding membranes. The advantage of this cylinder diameter engineering strategy lies in the uniform uniaxial lattice deformation of quasi-2D crystals and is readily applicable to tune other intriguing physical properties.

3. Conclusions

We have fabricated the highly crystalline and stoichiometric Fe_3N single films and heterostructures using the plasma-assisted PLD technique. The intrinsic magnetic and electronic phase transitions at a critical thickness of ≈5 u.c. were determined by the reduced dimensionality. The anomaly in the out-of-plane magnetic hysteresis loop was attributed to the reorientation of magnetic domains during field sweeping. Furthermore, we investigated the evolution of MR and AHE depending on the film thickness. The degeneracy in the in-plane magnetic responses and AHE signal reversal appeared as gradually increasing layer thickness. We attributed such behaviors to the band topology strongly associated with *k*-space Berry curvature, a typical character for ferromagnets with chiral spin texture. Finally, after field cooling to below the Néel temperature of CrN, a sizable in-plane exchange bias field of an AFM/FM heterointerface changed the sign. We demonstrated that the magnetic property of such a functional interface was highly tunable by modifying the diameter of the supporting sapphire cylinder in a large range. To this end, our work on manipulating the physical properties of high-quality nitride single films and all nitride heterostructures can be extended to various similar systems. Applying rare-earth-element-free nitrides with emergent magnetic properties will stimulate combination with other low-dimensional nanomaterials.

4. Experimental Section

Fabrication of High-Quality Samples: The Fe_3N thin films were fabricated by PLD assisted by radio-frequency plasma source supplying highly active nitrogen atoms. A stoichiometric ceramic Fe_3N target was synthesized using a high-pressure reaction route from a mixed $FeCl_3$ and $NaNH_2$ powder. The high-quality target fabrication was conducted at the High-Pressure Lab of South University of Science and Technology (SUSTech). This technique was used in a previous work and the details of fabrication process for the nitride bulk ceramics or single-crystals were described in previous works. The Fe_3N thin films were deposited at an optimized condition, that is, the substrate temperature of 400 °C, laser density of ≈1 J cm^{-2}, and base pressure of 1×10^{-8} Torr. The films were grown under a nitrogen plasma. The high purity N_2 gas was activated into nitrogen atoms by a radio frequency plasma source with input power varied from 100 to 250 W and partial pressure of N_2 gas varied from 10^{-4} to 10^{-5} Torr. The plasma source was equipped with a parallel plate capacitor to remove ionic species within the plasma. The samples were cooled down to room-temperature under the irradiation of nitrogen plasma in order to compensate the NVs. The CrN/Fe_3N bilayer and superlattices were fabricated under the same experimental conditions. The layer thickness was carefully controlled by counting the number of laser pulses and further confirmed by X-ray reflectivity measurements. The number of bilayer repeats was kept the same for all superlattices in order to maintain the identical number of interfaces.

Manipulation of Bending Curvatures of Fe_3N/CrN Freestanding Membranes Using Cylinder Diameter Engineering: The Fe_3N/CrN bilayers

were fabricated on the single-crystalline sodium chloride substrates under the same conditions. After the growth, the Fe_3N/CrN bilayers were immersed into the de-ionized water to dissolve the sodium chloride substrates. Then, the bilayers floated on the water surface. The sapphire cylinders with different curvatures (0, 0.1, and 0.25 mm^{-1}) were used to scoop up the Fe_3N/CrN freestanding membranes. Thus, the membranes attached to the sticks firmly. The samples were hot dried in the oven at 100 °C for 2 h. The membranes suffered the bending stress from sapphire cylinders with different curvatures. This led to the lattice deformation and successful tuning of magnetic properties of membranes.

Physical Properties Characterizations: The crystallinity of samples was checked by in-house high-resolution four-circle XRD using a Cu Kα_1 source (Panalytical MRD X'Pert 3). The microstructures of a Fe_3N single layer and a Fe_3N/CrN bilayer were examined using JEM ARM 200CF electron microscopy at the Institute of Physics, Chinese Academy of Sciences. Elemental-specific EELS mapping were performed at the Fe *L*-, Cr *L*-, N *k*-, and O *K*-edges from the interested regions after background subtracting. The magnetic properties of samples were characterized by a SQUID equipped with a high-temperature unit. Both in-plane and out-of-plane magnetization were obtained ranging from 10 to 500 K. The exchange bias was recorded at low temperatures after the sample was field-cooled down to 10 K under magnetic fields of ±3 T. The transport properties were performed using standard van der Pauw geometry with wire-bonding technique. The measurements were conducted using a 9T-PPMS. The AC current was kept at a minimum requirement of 1 μA to avoid the Joule heating. XPS measurements were performed at the Institute of Physics, Chinese Academy of Sciences. Spectra were collected at both Fe 2p and N 1s core-level peaks at room-temperature.

Room-Temperature Magneto–Optical Kerr Effect Measurements: The MOKE measurements were performed using a commercial MOKE microscope from Evico Magnetics. The evolution of the magnetic domain structures was imaged and recorded using a quasi-static technique. The images were taken simultaneously by sweeping magnetic fields. Both in-plane and out-of-plane fields were applied during the imaging.

Polarized Neutron Reflectivity Measurements: The PNR experiments on the Fe_3N/CrN superlattices were performed at the BL-4A of Spallation Neutron Source, Oak Ridge National Laboratory. An in-plane magnetic field of 0.5 T was applied during the measurements. The two superlattices were measured simultaneously at room temperature to avoid any arbitrary effects. The PNR measurements on a Fe_3N/CrN bilayer were conducted with the multipurpose reflectometer at the Chinese Spallation Neutron Source. In this experiment, an in-plane magnetic field of 1 T was applied during the sample cooling. The measurements were conducted at the same magnetic field at 10 K. In both PNR measurements, the specular reflectivities were recorded as a function of the wave factor transfer along the film surface normal. R^+ and R^- reflected the specular reflectivities from spin-up and spin-down polarized neutrons, respectively. The nuclear and magnetic scattering length densities were obtained simultaneously by fitting the PNR data using GenX software.

Supporting Information

Supporting Information is available from the Wiley Online Library or from the author.

Acknowledgements

This work was supported by the National Key Basic Research Program of China (Grant Nos. 2020YFA0309100 and 2019YFA0308500), the National Natural Science Foundation of China (Grant Nos. 11974390, 11721404, 11874412, and 12174437), the Beijing Nova Program of Science and Technology (Grant No. Z191100001119112), the Beijing Natural Science Foundation (Grant No. 2202060), the Guangdong-Hong Kong-Macao Joint Laboratory for Neutron Scattering Science and Technology, and the Strategic Priority Research Program (B) of the Chinese Academy of Sciences (Grant No. XDB33030200). The PNR experiments on a CrN/Fe_3N bilayer were conducted with multiple purpose reflectometry (MR) at the Chinese Spallation Neutron Source (CSNS) and the PNR experiments on the CrN/Fe_3N superlattices were conducted via a user proposal at Magnetism Reflectometer (BL-4A) at the Spallation Neutron Source (SNS), a DOE Office of Science user facility operated by Oak Ridge National Laboratory (ORNL).

Conflict of Interest

The authors declare no conflict of interest.

Data Availability Statement

The data that support the findings of this study are available from the corresponding author upon reasonable request.

Keywords

cylinder diameter engineering, exchange bias, Fe_3N, magnetic anisotropy

Received: September 7, 2022
Revised: October 19, 2022
Published online:

[1] O. Gutfleisch, M. A. Willard, E. Bruck, C. H. Chen, S. G. Sankar, J. P. Liu, *Adv. Mater.* **2011**, *23*, 821.
[2] B. Saha, A. Shakouri, T. D. Sands, *Appl. Phys. Rev.* **2018**, *5*, 021101.
[3] T. Mikolajick, S. Slesazeck, H. Mulaosmanovic, M. H. Park, S. Fichtner, P. D. Lomenzo, M. Hoffmann, U. Schroeder, *J. Appl. Phys.* **2021**, *129*, 100901.
[4] C. Rong, Y. Zhang, N. Poudyal, X. Xiong, M. J. Kramer, J. P. Liu, *Appl. Phys. Lett.* **2010**, *96*, 102513.
[5] S. A. Wolf, D. D. Awschalom, R. A. Buhrman, J. M. Daughton, S. von Molnar, M. L. Roukes, A. Y. Chtchelkanova, D. M. Treger, *Science* **2001**, *294*, 1488.
[6] R. S. Ningthoujam, N. S. Gajbhiye, *Prog. Mater. Sci.* **2015**, *70*, 50.
[7] R. Kumar, S. Nayak, M. Garbrecht, V. Bhatia, A. I. K. Pillai, M. Gupta, S. M. Shivaprasad, B. Saha, *J. Appl. Phys.* **2021**, *129*, 055305.
[8] G. Serghiou, G. Ji, N. Odling, H. J. Reichmann, D. J. Frost, J. P. Wright, *High Pressure Res* **2015**, *35*, 28.
[9] A. Fuertes, *APL Mater.* **2020**, *8*, 020903.
[10] C.-C. Chiang, V. Ostwal, P. Wu, C.-S. Pang, F. Zhang, Z. Chen, J. Appenzeller, *Appl. Phys. Rev.* **2021**, *8*, 021306.
[11] B. Anasori, M. R. Lukatskaya, Y. Gogotsi, *Nat. Rev. Mater.* **2017**, *2*, 16098.
[12] F. I. Ajami, R. K. Maccrone, *J. Phys. Chem. Solids* **1975**, *36*, 7.
[13] Y. Zhang, N. Haberkorn, F. Ronning, H. Wang, N. A. Mara, M. Zhuo, L. Chen, J. H. Lee, K. J. Blackmore, E. Bauer, A. K. Burrell, T. M. McCleskey, M. E. Hawley, R. K. Schulze, L. Civale, T. Tajima, Q. Jia, *J. Am. Chem. Soc.* **2011**, *133*, 20735.
[14] P. Wang, D. Wang, N. M. Vu, T. Chiang, J. T. Heron, Z. Mi, *Appl. Phys. Lett.* **2021**, *118*, 223504.
[15] S. Yasuoka, T. Shimizu, A. Tateyama, M. Uehara, H. Yamada, M. Akiyama, Y. Hiranaga, Y. Cho, H. Funakubo, *J. Appl. Phys.* **2020**, *128*, 114103.

[16] S. Fichtner, N. Wolff, F. Lofink, L. Kienle, B. Wagner, *J. Appl. Phys.* **2019**, *125*, 114103.
[17] Seema, D. Kumar , U. P. Deshpande, M. Gupta, *J. Appl. Phys.* **2021**, *130*, 125106.
[18] A.-M. Zieschang, J. D. Bocarsly, M. Dürrschnabel, H.-J. Kleebe, R. Seshadri, B. Albert, *Chem. Mater.* **2018**, *30*, 1610.
[19] T. K. Kim, M. Takahashi, *Appl. Phys. Lett.* **1972**, *20*, 492.
[20] T. Waki, S. Terazawa, Y. Tabata, K. Sato, A. Kondo, K. Kindo, H. Nakamura, *Phys. Rev. B* **2014**, *90*, 014416.
[21] N. Ji, L. F. Allard, E. Lara-Curzio, J.-P. Wang, *Appl. Phys. Lett.* **2011**, *98*, 092506.
[22] P. Wojciechowski, M. Lewandowski, *Cryst. Growth Des.* **2022**, *22*, 4618.
[23] K. Yamaguchi, T. Yui, K. Yamaki, I. Kakeya, K. Kadowaki, T. Suemasu, *J. Cryst. Growth* **2007**, *301*, 597.
[24] L.-Y. Yuan, L. Ma, W. He, H.-Y. Wu, Y.-B. Sun, C. Wen, G.-K. Li, C.-M. Zhen, J.-J. Shen, J.-J. Zhao, Y. Lu, D.-L. Hou, *J. Alloys Compd.* **2019**, *789*, 730.
[25] H. Fang, R. Zhang, B. Liu, Z. Tao, X. Wang, Z. Xie, X. Xiu, Y. Zheng, *J. Phys. D: Appl. Phys.* **2012**, *45*, 315002.
[26] H. Fang, J. Chen, X. Peng, Y. Li, Z. Tao, *Mater. Lett.* **2018**, *233*, 191.
[27] Y. H. Cheng, R. K. Zheng, H. Liu, Y. Tian, Z. Q. Li, *Phys. Rev. B* **2009**, *80*, 174412.
[28] A.-M. Zieschang, J. D. Bocarsly, M. Dürrschnabel, L. Molina-Luna, H.-J. Kleebe, R. Seshadri, B. Albert, *Chem. Mater.* **2017**, *29*, 621.
[29] S. Leone, J. Ligl, C. Manz, L. Kirste, T. Fuchs, H. Menner, M. Prescher, J. Wiegert, A. Žukauskaitė, R. Quay, O. Ambacher, *Phys Status Solidi Rapid Res Lett* **2019**, *14*, 1900535.
[30] Y. H. Liu, K. Wang, W. Lin, A. Chinchore, M. Shi, J. Pak, A. R. Smith, C. Constantin, *Thin Solid Films* **2011**, *520*, 90.
[31] A. Garzon-Fontecha, H. A. Castillo, E. Restrepo-Parra, W. De La Cruz, *Surf. Coat. Technol.* **2018**, *334*, 98.
[32] Q. Jin, H. Cheng, Z. Wang, Q. Zhang, S. Lin, M. A. Roldan, J. Zhao, J. O. Wang, S. Chen, M. He, C. Ge, C. Wang, H. B. Lu, H. Guo, L. Gu, X. Tong, T. Zhu, S. Wang, H. Yang, K. J. Jin, E. J. Guo, *Adv. Mater.* **2021**, *33*, 2005920.
[33] Q. Jin, Z. Wang, Q. Zhang, Y. Yu, S. Lin, S. Chen, M. Qi, H. Bai, A. Huon, Q. Li, L. Wang, X. Yin, C. S. Tang, A. T. S. Wee, F. Meng, J. Zhao, J.-o. Wang, H. Guo, C. Ge, C. Wang, W. Yan, T. Zhu, L. Gu, S. A. Chambers, S. Das, T. Charlton, M. R. Fitzsimmons, G.-Q. Liu, S. Wang, K.-j. Jin, et al, *Phys. Rev. Lett.* **2022**, *128*, 017202.
[34] Q. Jin, Z. Wang, Q. Zhang, J. Zhao, H. Cheng, S. Lin, S. Chen, S. Chen, H. Guo, M. He, C. Ge, C. Wang, J.-O. Wang, L. Gu, S. Wang, H. Yang, K.-j. Jin, E.-J. Guo, *Phys. Rev. Mater.* **2021**, *5*, 023604.
[35] Q. Jin, J. Zhao, M. A. Roldan, W. Qi, S. Lin, S. Chen, H. Hong, Y. Fan, D. Rong, H. Guo, C. Ge, C. Wang, J.-O. Wang, S. Wang, K.-j. Jin, E.-J. Guo, *Appl. Phys. Lett.* **2022**, *120*, 073103.
[36] A. Filippetti, N. A. Hill, *Phys. Rev. Lett.* **2000**, *85*, 5166.
[37] C. X. Quintela, J. P. Podkaminer, M. N. Luckyanova, T. R. Paudel, E. L. Thies, D. A. Hillsberry, D. A. Tenne, E. Y. Tsymbal, G. Chen, C. B. Eom, F. Rivadulla, *Adv. Mater.* **2015**, *27*, 3032.
[38] A. Leineweber, H. Jacobs, F. Huning, H. Lueken, H. Schilder, W. Kockelmann, *J. Alloys Compd.* **1999**, *288*, 79.
[39] S. Matar, B. Siberchicot, M. Penicaud, G. Demazeau, *J. Phys. I* **1992**, *2*, 1819.
[40] E. J. Miola, S. D. de Souza, P. A. P. Nascente, M. Olzon-Dionysio, C. A. Olivieri, D. Spinelli, *Appl. Surf. Sci.* **1999**, *144*, 272.
[41] J. W. Arblaster, *Johnson Matthey Technol. Rev.* **2015**, *59*, 174.
[42] F. Seitz, *The Modern Theory of Solids*, Dover Publications, Mineola, NY, USA **1987**, p. 10.
[43] M. Huuijben, L. W. Martin, Y. H. Chu, M. B. Holcomb, P. Yu, G. Rijnders, D. H. A. Blank, R. Ramesh, *Phys. Rev. B* **2008**, *78*, 094413.
[44] J. Xia, W. Siemons, G. Koster, M. R. Beasley, A. Kapitulnik, *Phys. Rev. B* **2009**, *79*, 140407(R).
[45] R. Scherwitzl, S. Gariglio, M. Gabay, P. Zubko, M. Gibert, J.-M. Triscone, *Phys. Rev. Lett.* **2011**, *106*, 246403.
[46] P. D. C. King, H. I. Wei, Y. F. Nie, M. Uchida, C. Adamo, S. Zhu, X. He, I. Božović, D. G. Schlom, K. M. Shen, *Nat. Nanotech.* **2014**, *9*, 443.
[47] J. Fowlie, M. Gibert, G. Tieri, A. Gloter, J. Íñiguez, A. Filippetti, S. Catalano, S. Gariglio, A. Schober, M. Guennou, J. Kreisel, O. Stéphan, J.-M. Triscone, *Adv. Mater.* **2017**, *29*, 1605197.
[48] X. Y. Zhang, J. S. Chawla, B. M. Howe, D. Gall, *Phys. Rev. B* **2011**, *83*, 165205.
[49] C. Leighton, J. Nogues, H. Suhl, I. K. Schuller, *Phys. Rev. B* **1999**, *60*, 12837.
[50] M. R. Fitzsimmons, C. Dufour, K. Dumesnil, J. Dou, M. Pechan, *Phys. Rev. B* **2009**, *79*, 144425.
[51] J. Matsuno, N. Ogawa, K. Yasuda, F. Kagawa, W. Koshibae, N. Nagaosa, Y. Tokura, M. Kawasaki, *Sci. Adv.* **2016**, *2*, e1600304.
[52] H. Tsai, T. Higo, K. Kondou, T. Nomoto, A. Sakai, A. Kobayashi, T. Nakano, K. Yakushiji, R. Arita, S. Miwa, Y. Otani, S. Nakatsuji, *Nature* **2020**, *580*, 608.
[53] L. Wang, Q. Feng, Y. Kim, R. Kim, K. H. Lee, S. D. Pollard, Y. J. Shin, H. Zhou, W. Peng, D. Lee, W. Meng, H. Yang, J. H. Han, M. Kim, Q. Lu, T. W. Noh, *Nat. Mater.* **2018**, *17*, 1087.
[54] K. Y. Meng, A. S. Ahmed, M. Bacani, A. O. Mandru, X. Zhao, N. Bagues, B. D. Esser, J. Flores, D. W. McComb, H. J. Hug, F. Yang, *Nano Lett.* **2019**, *19*, 3169.
[55] J. Tang, L. Kong, W. Wang, H. Du, M. Tian, *Chin. Phys. B* **2019**, *28*, 087503.
[56] H. Zhu, Y. Wang, J. Xiao, M. Liu, S. Xiong, Z. J. Wong, Z. Ye, Y. Ye, X. Yin, X. Zhang, *Nat. Nanotechnol.* **2015**, *10*, 151.
[57] M. Zeng, J. Liu, L. Zhou, R. G. Mendes, Y. Dong, M. Y. Zhang, Z. H. Cui, Z. Cai, Z. Zhang, D. Zhu, T. Yang, X. Li, J. Wang, L. Zhao, G. Chen, H. Jiang, M. H. Rümmeli, H. Zhou, L. Fu, *Nat. Mater.* **2020**, *19*, 528.
[58] H. Yao, K. Jin, Z. Yang, Q. Zhang, W. Ren, S. Xu, M. Yang, L. Gu, E. J. Guo, C. Ge, C. Wang, X. Xu, D. Zhang, G. Yang, *Adv. Mater. Interfaces* **2021**, *8*, 2101499.